

A thermo-mechanical terrestrial model of Arctic coastal erosion

Jennifer Frederick¹, Alejandro Mota¹, Irina Tezaur^{1,*}, Diana Bull¹

¹ Sandia National Laboratories, Albuquerque, NM and Livermore, CA, USA.

*Corresponding author: ikalash@sandia.gov

Abstract. Although the Arctic comprises one-third of the global coastline and has some of the fastest eroding coasts, current tools for quantifying permafrost erosion are unable to explain the episodic, storm-driven erosion events that occur in this region. In this paper, we present a novel multi-physics finite element model for the numerical simulation of Arctic coastal permafrost degradation: the terrestrial component of the Arctic Coastal Erosion (ACE) model. This model is comprised of two main ingredients: (1) a solid mechanics model that calculates the three-dimensional (3D) stress, strain and displacement fields of the underlying permafrost developing in response to a frozen water content dependent plasticity model, and (2) a novel thermal model governing the 3D heat conduction and solid-liquid phase change occurring within the permafrost. These two physics sets are coupled via a sequential thermo-mechanical coupling scheme developed within the ALBANY LCM open-source finite element code. Unlike prior approaches, our modeling methodology enables failure from *any* allowable deformation (block failure, thermo-denudation, thermo-abrasion); moreover, failure modes develop from constitutive (rather than empirical) relationships inherent in the underlying finite element model. Elements are dynamically removed from the underlying finite element mesh so as to simulate transient permafrost erosion events. Our thermo-mechanical terrestrial model is evaluated on a pseudo-realistic problem in which a slice of permafrost is exposed to realistic oceanic and atmospheric forcing boundary condition data occurring at Drew Point, Alaska in July 2018.

Keywords. Thermal, mechanics, coupling, Arctic coastal erosion, permafrost.

1. Introduction

The Arctic coastline comprises one-third of the global coastline length and is retreating at an average rate of 0.5 m/yr [22]. Arctic coastlines are unique in that they are composed of permafrost, defined as ground (soil, rock, and/or sediment) that remains frozen for two or more consecutive years. Ice in permafrost acts as the consolidating material (Figure 1), making erosion in the Arctic fundamentally a thermal-chemical-mechanical process for which models developed for the lower latitudes have limited applicability. Thermo-denudation and thermo-abrasion processes dominate Arctic coastal erosion [2, 39, 15]. Thermo-denudation refers to the degradation of permafrost from warming air causing subsidence or slumping under gravitational forces. With a thermo-abrasive process, undercutting of a permafrost bluff to produce a recess or niche occurs as the permafrost is first warmed by the ocean and then removed by the mechanical action of waves. The resulting over-hanging bluff then fails in a “block failure” event (Figure 1).

The permafrost thermal state, and hence ice saturation, is known to be a first order control on the strength of the permafrost [3] and has thus been the basis of most niche development models. Kobayashi [20] developed a one-dimensional (1D) analytical solution for heat transfer from the ocean considering water temperature, water level, and water dwell time in order to predict niche depth [20]. Empirical equations originally designed to predict the melting rate of free-drifting icebergs (e.g., [34, 42]) have also been the basis of niche formation predictions [43, 4]. While the ocean is recognized as the cause of the niche formation, only [31, 4] worked to establish somewhat realistic oceanographic boundary conditions to drive niche development.

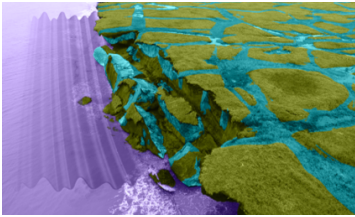


FIGURE 1. Aerial photograph of block failure along the Arctic coastline. Ice wedges are enhanced with blue, ocean with purple, and permafrost with green.

expanded upon [17, 18] by evaluating the three-dimensional (3D) stress states in an elastic mechanical model of Arctic coastal permafrost implemented within the ALBANY LCM finite element code. The location and magnitude of the simulated maximum tensile stress (a key metric that reflects a likely initiation location for block failure) were evaluated for various geometric (bluff height, ice wedge polygon size, ice wedge geometry) and material (bulk density, Young’s modulus, Poisson’s ratio) parameters.

The present work is unique in that we model the mechanical strength of the entire permafrost bluff as a function of its thermal state in a novel multi-physics finite element model for the numerical simulation of Arctic coastal permafrost degradation. At the heart of this model is a strain and displacement field underlying the permafrost coupled to a novel thermal model governing the 3D heat conduction and solid-liquid phase change occurring within the permafrost. The thermal state is forced using realistic atmospheric and oceanic boundary conditions. The present mechanical formulation expands upon our earlier mechanical model [36] to include plasticity and to incorporate all the mechanisms that lead to the deformation. Together the combined terrestrial, oceanographic, and atmospheric components constitute the Arctic Coastal Erosion (ACE) model; this paper focuses on the developments in thermo-mechanical treatment of the terrestrial portion of this model. Unlike previous models, the new modeling framework enables failure from any allowable deformation (block failure, thermo-denudation, thermo-abrasion), and derives failure modes from constitutive relationships inherent in the underlying physics, rather than pre-determined failure planes, approximations of the boundary conditions, critical niche depth, or empirical relationships.

The permafrost thermal state controls the strength for the entire permafrost bluff, not just the niche, and is the root cause of overall bluff instability. However, previous work on bluff instability focused on analytical relationships to explore how sliding versus toppling failure modes are influenced by geomorphological (niche depth, ice-wedge geometries, bluff heights) and geophysical (ice content, sediment shear strength) properties assuming, if an ice-wedge is present, that the failure will occur along that plane [17, 18]. Our earlier work [36] ex-

The remainder of this paper is organized as follows. In Sections 2 and 3, we introduce formulations for the two problems comprising our model, the solid mechanics problem and the thermal problem, respectively. In Section 4, we discuss the material models developed for the specific case of Arctic ice and permafrost embedded in these two formulations and through which the solid mechanics and thermal problems are coupled. Section 5 describes the criteria and methodology for erosion of permafrost material. Implementation of the thermo-mechanical terrestrial model within the ALBANY LCM multi-physics finite element code and the sequential algorithm for coupling the physics are detailed in Section 6. We provide numerical results on a pseudo-realistic problem informed by realistic atmospheric and oceanographic data in Section 7. A concluding summary and a discussion of future work is given in Section 8.

2. Formulation of the solid mechanics problem

We begin by providing the standard finite deformation variational formulation for the solid mechanics problem, the first ingredient in our ACE thermo-mechanical terrestrial model. It defines the permafrost stresses and displacements.

Let $I := \{t \in [t_0, t_1]\}$ be a closed time interval with $0 \leq t_0 < t_1$, and $t_0, t_1 \in \mathbb{R}$, and consider a body as the regular open set $\Omega \subset \mathbb{R}^3$ undergoing a motion described by the mapping $\mathbf{x} = \varphi(\mathbf{X}, t) : \Omega \times I \rightarrow \mathbb{R}^3$, where $\mathbf{X} \in \Omega$ and $t \in I$. Assume that the boundary of the body is $\Gamma = \partial_\varphi\Omega \cup \partial_{\mathbf{T}}\Omega$, where $\partial_\varphi\Omega$ is a prescribed position boundary, $\partial_{\mathbf{T}}\Omega$ is a prescribed traction boundary, and $\partial_\varphi\Omega \cap \partial_{\mathbf{T}}\Omega = \emptyset$. The prescribed boundary positions or Dirichlet boundary conditions are $\boldsymbol{\chi} : \partial_\varphi\Omega \times I \rightarrow \mathbb{R}^3$. The prescribed boundary tractions or Neumann boundary conditions are $\mathbf{T} : \partial_{\mathbf{T}}\Omega \times I \rightarrow \mathbb{R}^3$. Let $\mathbf{F} := \text{Grad } \varphi$ be the deformation gradient. Let the initial position and velocity at time t_0 be $\mathbf{x}_0 \equiv \mathbf{X} : \Omega \rightarrow \mathbb{R}^3$, and $\mathbf{v}_0 : \Omega \rightarrow \mathbb{R}^3$, correspondingly. Let also $\rho_0 \mathbf{B} : \Omega \rightarrow \mathbb{R}^3$ be the body force, with ρ_0 the mass density in the reference configuration. Furthermore, introduce the kinetic energy of the body as

$$T(\dot{\varphi}) := \frac{1}{2} \int_{\Omega} \rho_0 \dot{\varphi} \cdot \dot{\varphi} \, dV, \quad (2.1)$$

and its potential energy as

$$V(\varphi) := \int_{\Omega} A(\mathbf{F}, \mathbf{Z}) \, dV - \int_{\Omega} \rho_0 \mathbf{B} \cdot \varphi \, dV - \int_{\partial_{\mathbf{T}}\Omega} \mathbf{T} \cdot \varphi \, dS, \quad (2.2)$$

in which $A(\mathbf{F}, \mathbf{Z})$ is the Helmholtz free-energy density and \mathbf{Z} is a collection of internal variables. The Lagrangian function of the body is then $L(\varphi, \dot{\varphi}) := T(\dot{\varphi}) - V(\varphi)$, which gives rise to the action functional $S[\varphi] := \int_I L(\varphi, \dot{\varphi}) \, dt$. According to the Variational Principle of Hamilton, the equation of motion is obtained by finding the critical point of the action functional $S[\varphi]$ over the Sobolev space $W_2^1(\Omega \times I)$ that is comprised of all functions that are square-integrable and have square-integrable first derivatives, for fixed endpoints of the deformation mapping at t_0 and t_1 [24]. Define $\mathcal{S} := \{\varphi \in W_2^1(\Omega \times I) : \varphi = \boldsymbol{\chi} \text{ on } \partial_\varphi\Omega \times I; \varphi = \mathbf{x}_0 \text{ on } \Omega \times t_0; \varphi = \mathbf{x}_1 \text{ on } \Omega \times t_1\}$ and $\mathcal{V} := \{\boldsymbol{\xi} \in W_2^1(\Omega \times I) : \boldsymbol{\xi} = \mathbf{0} \text{ on } \partial_\varphi\Omega \times I \cup \Omega \times t_0 \cup \Omega \times t_1\}$, where $\boldsymbol{\xi}$

is a test function. This leads to

$$\delta S := DS[\varphi](\xi) = \int_I \left[\int_{\Omega} (\text{Div } \mathbf{P} + \rho_0 \mathbf{B} - \rho_0 \ddot{\varphi}) \cdot \xi \, dV + \int_{\partial_T \Omega} \mathbf{T} \cdot \xi \, dS \right] dt = 0, \quad (2.3)$$

where $\mathbf{P} = \partial A / \partial \mathbf{F}$ denotes the first Piola-Kirchhoff stress. The Euler-Lagrange equation corresponding to (2.3) is then

$$\text{Div } \mathbf{P} + \rho_0 \mathbf{B} = \rho_0 \ddot{\varphi} \quad \text{in } \Omega \times I, \quad (2.4)$$

with initial and boundary conditions given respectively by:

$$\begin{aligned} \varphi(\mathbf{X}, t_0) &= \mathbf{x}_0, \quad \dot{\varphi}(\mathbf{X}, t_0) = \mathbf{v}_0 \quad \text{in } \Omega, \\ \varphi(\mathbf{X}, t) &= \chi \quad \text{on } \partial_{\varphi} \Omega \times I, \quad \mathbf{P} \mathbf{N} = \mathbf{T} \quad \text{on } \partial_T \Omega \times I. \end{aligned} \quad (2.5)$$

The variational statement (2.3) is discretized in space using the finite element method with isoparametric basis functions (linear 8-node hexahedrons, as discussed in Section 7) and in time using a Newmark time-integration scheme [19]. We defer discussion of the specific values for the boundary condition and body force terms appearing in equations (2.4) and (2.5) until the numerical results section, Section 7.

3. Formulation of the thermal problem

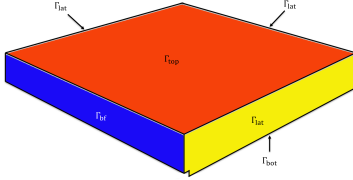


FIGURE 2. Example bluff geometry illustrating the four relevant boundaries: Γ_{bf} (blue), Γ_{top} (red), Γ_{bot} and Γ_{lat} (yellow).

Having introduced the solid mechanics problem, we now turn our attention to the thermal problem, the second component in the ACE thermo-mechanical terrestrial model. Here, we utilize the governing equation for heat transfer by conduction in a saturated porous media including water-ice phase change, described by

$$\overline{\rho c_p} \frac{\partial T}{\partial t} = \nabla \cdot (\mathbf{K} \cdot \nabla T) + \Theta, \quad \text{in } \Omega, \quad (3.1)$$

where $\Omega \subset \mathbb{R}^3$ is a smooth bounded domain, ρ is the density, c_p is the specific heat, T is the temperature, \mathbf{K} is the thermal diffusivity tensor, and Θ is the heat source term due to phase change (latent heat). The bar over the term $\overline{\rho c_p}$ indicates a volume-averaged mixture model for the density and specific heat of each material component. The possible material components include water and ice in the pore space, θ , and sediment-based rock mineral grains (e.g., sand, silt, clay) in the solid, $1 - \theta$. Effective porosity is defined as $\theta = V_{\text{void}} / V_{\text{total}}$, the ratio of the void volume V_{void} to the total volume V_{total} . The water saturation, w , and ice saturation, f , are defined as the fraction of water or ice occupying the effective pore space, respectively, and can vary from 0 to 1. The volume fraction of each material component occupying the effective pore space is $S_f = \theta f$ for ice, and $S_w = \theta w$ for water. The mixture models for each thermal parameter are further described in Section 4.2. The source term Θ in (3.1) is defined according to

$$\Theta := \rho_f L_f \frac{\partial f}{\partial t} = \rho_f L_f \frac{\partial f}{\partial T} \frac{\partial T}{\partial t}, \quad (3.2)$$

where ρ_f is ice density and L_f is the latent heat of water-ice phase change. The function $\frac{\partial f}{\partial T}$ represents the sediment freezing curve and describes how ice saturation changes with temperature. This function is non-zero only during phase change, and is further described in Section 4.2. For numerical stability, the heat source term is reformulated as a correction to the heat storage term,

$$\overline{\rho c_p'} := \overline{\rho c_p} - \rho_f L_f \frac{\partial f}{\partial T}, \quad (3.3)$$

thus modifying (3.1) to,

$$\left[\overline{\rho c_p} - \rho_f L_f \frac{\partial f}{\partial T} \right] \frac{\partial T}{\partial t} - \nabla \cdot (\mathbf{K} \cdot \nabla T) = 0. \quad (3.4)$$

This is commonly known as the apparent heat capacity method, which is a classical approach used in heat transfer problems where conduction is the dominant process [1]. To complete the definition of the thermal equation (3.4), we must provide boundary conditions on the boundary of Ω , which we denote by Γ . Let us decompose the boundary Γ as $\Gamma = \Gamma_{\text{bf}} \cup \Gamma_{\text{top}} \cup \Gamma_{\text{bot}} \cup \Gamma_{\text{lat}}$. Here, Γ_{bf} denotes the bluff face, Γ_{top} denotes the bluff top, Γ_{bot} denotes the bluff bottom, and Γ_{lat} denotes the remaining three lateral boundaries of the bluff, not including the bluff face (see Figure 2). The relevant boundary conditions for the thermal problem are as follows:

$$\mathbf{K} \frac{\partial T(t)}{\partial z} = -\mathbf{q}(t) \text{ on } \Gamma_{\text{bot}}, \quad \mathbf{K} \frac{\partial T(t)}{\partial x} = \mathbf{K} \frac{\partial T(t)}{\partial y} = \mathbf{0} \text{ on } \Gamma_{\text{lat}}, \quad (3.5)$$

$$T(t) = T_{\text{air}}(t) \text{ on } \Gamma_{\text{top}}, \quad T(t) = \begin{cases} T_{\text{air}}(t), & \text{on } \Gamma_{\text{bf}} \text{ if exposed} \\ T_{\text{ocean}}(t), & \text{on } \Gamma_{\text{bf}} \text{ if submerged} \end{cases} \quad (3.6)$$

In (3.5), $\mathbf{q}(t) := \mathbf{K} \cdot \nabla T$ denotes the heat flux, and in (3.6), $T_{\text{air}}(t)$ and $T_{\text{ocean}}(t)$ are the prescribed air and ocean temperatures at the bluff face. The values for these boundary conditions are defined by appropriate environmental data applied to the thermal model, and realistic values for Drew Point, Alaska are provided in Section 7.

It is straightforward to obtain the weak variational form of (3.4):

$$\int_{\Omega} \left(\overline{\rho c_p} - \rho_f L_f \frac{df}{dT} \right) \frac{\partial T}{\partial t} \boldsymbol{\xi} \, dV + \int_{\Omega} (\mathbf{K} \cdot \nabla T) \nabla \boldsymbol{\xi} \, dV - \int_{\Gamma} \boldsymbol{\xi} \mathbf{q} \cdot \mathbf{n} \, dS = 0, \quad (3.7)$$

where $\boldsymbol{\xi} \in \mathcal{V}$ is a square-integrable test function having a square-integrable first derivative, and \mathbf{n} denotes the normal vector to Γ . As is Section 2, the variational statement (3.7) is discretized in space using standard isoparametric finite element shape functions (linear 8-node hexahedrons, as discussed in Section 7). We advance (3.7) forward in time using a Forward Euler time-stepping scheme.

4. Material models

In this section, we describe the material models used for capturing the behavior of ice and permafrost, the relevant materials in our ACE terrestrial model. A unique feature of the ACE model is that the coupling between the thermal and mechanical components happens at the level of the material, as demonstrated below.

4.1. Mechanical material models

4.1.1. Constitutive model for ice. We begin by discussing our constitutive model for ice, which is extended to permafrost in Section 4.1.2 below.

It is well-known that ice is a polycrystalline granular material. Its microstructure can evolve under different stress states due to plastic deformation, recrystallization, and grain boundary migration [11]. Its material response is highly nonlinear, viscoplastic and anisotropic, depending mainly on applied stress, strain-rate, temperature, salinity, grain-size, and anisotropic effects [37]. While mostly brittle under tension, it undergoes transitions to a ductile material under significant compression. We model the mechanical response of ice using standard J_2 plasticity extended to the large-deformation regime for several reasons. First, our application space is at a sufficiently large scale, and therefore the micro-structural characteristics of ice are reasonably captured by an isotropic material model. Second, it incorporates all the mechanisms that lead to the deformation, plastic flow of polycrystalline materials like ice. Additionally, it requires minimal calibration (most parameters are determined by the known crystalline microstructure of ice), and is implemented within the ALBANY LCM code where our erosion framework resides (Section 6.2).

For the sake of brevity, we discuss here several relevant concepts from J_2 -flow theory as relevant to our particular application. For a detailed derivation of the relevant material modeling framework, the reader is referred to Appendix A of [6].

The thermo-mechanical response of the solids considered here is characterized by a free-energy density per unit undeformed volume of the form $A = A(\mathbf{F}, \mathbf{F}^p, \epsilon^p, T)$ where \mathbf{F} is the deformation gradient, \mathbf{F}^p is the plastic part of the deformation gradient, $\epsilon^p \geq 0$ is an effective deviatoric plastic strain, T is the absolute temperature, and $\mathbf{F}^e = \mathbf{F}(\mathbf{F}^p)^{-1}$ is the elastic part of the deformation gradient [23]. We assume that the free-energy density A has the additive structure

$$A(\mathbf{F}, \mathbf{F}^p, \epsilon^p, T) = W^e(\mathbf{F}^e, T) + W^p(\epsilon^p, T), \quad (4.1)$$

where $W^e(\mathbf{F}^e, T)$ and $W^p(\epsilon^p, T)$ are the elastic and stored energy densities per unit undeformed volume, respectively. We denote by $\boldsymbol{\sigma}$ the stress conjugate to ϵ^e , namely $\boldsymbol{\sigma} := \partial W^e / \partial \epsilon^e$. We assume that the plastic deformation of the ice matrix leaves the elastic properties of the matrix unchanged. This assumption is appropriate for crystalline materials such as ice, whose elastic properties are ostensibly insensitive to isochoric plastic deformation. A simple form of the resulting elastic energy is

$$\begin{aligned} W^e(\epsilon^e, T) &= W^{e,\text{vol}}(\theta^e, T) + W^{e,\text{dev}}(\epsilon^e, T), \\ W^{e,\text{vol}}(\theta^e, T) &= \frac{K}{2} [\theta^e - \alpha(T - T_0)]^2, \quad W^{e,\text{dev}}(\epsilon^e, T) = \mu \|\text{dev}(\epsilon^e)\|^2, \end{aligned} \quad (4.2)$$

where $\theta^e = \log J^e$, K is the bulk modulus, μ is the shear modulus, α is the thermal expansion coefficient, T_0 is a reference absolute temperature, and $J^e := \det(\mathbf{F}^e)$. In practice, the Young's modulus E and the Poisson's ratio ν are used, and they are related to the bulk and shear moduli by $K = \frac{E}{3(1-2\nu)}$ and $\mu = \frac{E}{2(1+\nu)}$.

A simple stored energy function can be formulated by assuming a deviatoric character to the plasticity. This can be modeled simply by a conventional power-law

of hardening such that the effective yield stress is

$$\sigma_{\text{eff}}(T) := \sqrt{\frac{2}{3}} \sigma_0(T) + K_{\text{hard}} \epsilon^p + K_{\text{sat}} [1 - \exp(-k \epsilon^p)]. \quad (4.3)$$

In this expression, $\sigma_0(T)$ is the reference yield stress, K_{hard} is a hardening modulus, K_{sat} is a saturation modulus, and k is a saturation exponent. The reference yield stress is assumed to depend on temperature through the ice saturation, as follows

$$\sigma_0(T) := f(T) \sigma_Y^{\text{ice}}. \quad (4.4)$$

Here, $f(T) \in [0, 1]$ is the ice saturation, computed separately by the thermal problem described in Section 3 and coupled to the mechanical problem as described in Section 6, and σ_Y^{ice} is the yield stress of pure crystalline ice.

4.1.2. Constitutive model for permafrost. The mechanical behavior of permafrost at the surveyed sites is mostly characterized by its ice content, and it only shows a significant deviation from elasto-perfectly-plastic behavior near the melting point of ice, according to our experiments [9, 6]. Near the melting point of ice the softening behavior exhibited by the stress-strain relationship may be appropriately modeled by a hardening law such as Voce or power law. For these reasons, we assume that the mechanical behavior of permafrost may also be captured by the same J_2 -flow plasticity model we introduced for ice. The yield stress (4.4), however, is now expressed as

$$\sigma_0(T) := \sigma_Y^{\text{sediment}} + f(T) \sigma_Y^{\text{ice-sediment}} \quad (4.5)$$

where $\sigma_Y^{\text{sediment}}$ and $\sigma_Y^{\text{ice-sediment}}$ are the values of the yield stresses of the sediment and ice-sediment interface, respectively, and $f(T)$ is the ice saturation.

4.2. Thermal material models

The thermal material model defines the bulk values of density, specific heat, and thermal conductivity, as well as the sediment freezing curve $\frac{\partial f}{\partial T}$, based on the material constituents (ice, water, and sediment component fractions). A mixture model for the bulk-averaged density and specific heat (denoted by an over-bar) is then defined as

$$\bar{\rho} = S_f \rho_f + S_w \rho_w + (1 - \theta) \rho_s, \quad (4.6)$$

where ρ_w and ρ_s are the densities of water and rock mineral grains (sediment), respectively, and

$$\bar{c}_p = S_f c_{p_f} + S_w c_{p_w} + (1 - \theta) c_{p_s}, \quad (4.7)$$

where c_{p_f} , c_{p_w} , and c_{p_s} are the specific heats of ice, water and sediment, respectively.

The thermal conductivity tensor \mathbf{K} can account for anisotropic materials; however, here we assume isotropic behavior, so that $\mathbf{K} := \kappa \mathbf{I}$, where \mathbf{I} is an identity matrix, and $\kappa > 0$ is the isotropic value of the thermal conductivity. The mixture model for the bulk-averaged thermal conductivity $\bar{\kappa}$ is not a simple volume-average of the thermal diffusivity of each material component since the connected structure of the solid phase components can conduct heat more favorably than the materials in the pore space. It is defined using a mixing rule as

$$\bar{\kappa} = \kappa_f^{S_f} \kappa_w^{S_w} \kappa_s^{(1-\theta)} \quad (4.8)$$

where κ_f , κ_w and κ_s are the thermal conductivities of ice, water and sediment, respectively, and the superscripts denote exponentiation. The values for ρ_s , c_{p_s} , and κ_s can be calculated with knowledge of the sediment composition and is based on a simple volume averaged mixing model,

$$\zeta_s = F_{\text{peat}}\zeta_{\text{peat}} + F_{\text{sand}}\zeta_{\text{sand}} + F_{\text{silt}}\zeta_{\text{silt}} + F_{\text{clay}}\zeta_{\text{clay}}, \quad (4.9)$$

where ζ represents either ρ , c_p , or κ , and F_i denotes the peat, sand, or silt fraction in the sediment mixture, depending on $i \in \{\text{peat, sand, silt, clay}\}$. The values for each constituent are given in Table 1.

TABLE 1. Thermal properties of permafrost constituents. Values guided by [33],[30],[14].

constituent i	ρ_i [kg/m ³]	c_{p_i} [J/kg/K]	κ_i [W/K/m]	v_i
peat	250	1.9×10^3	0.08	5.0
sand	2600	0.7×10^3	8.0	5.0
silt	2500	0.7×10^3	4.9	25.0
clay	2350	0.6×10^3	0.4	70.0
ice	920	2.09×10^3	1.6	—
water	1000	4.18×10^3	0.58	—

The freezing of saturated sediment is a very complex process and depends on a number of factors, including but not limited to pore fluid salinity, sediment type, and pore size. In general, pore water freezing is mainly determined by the solution properties for pores larger than $0.2 \mu\text{m}$, but for pores smaller than $0.2 \mu\text{m}$, the effect of pore size on water freezing becomes important [40]. Experimental studies by Darrow et al. (2009) [13], Darrow (2011) [12], and Kruse & Darrow (2017) [21] are used as the basis for sediment freezing curves for clay and silt. Furthermore because of the large pore size for sand and peat, we assume a narrow freezing curve width of approximately 4°C . A generalized logistic curve is used to describe the sediment freezing curve, which gives the ice saturation, f , as a function of current temperature, T , and freezing temperature, T_f :

$$f(T, T_f) = A + \frac{D - A}{(C + Qe^{-G(T - T_f)})^{1/v_{\text{bulk}}}}. \quad (4.10)$$

The parameters in (4.10) control the general shape of the freezing curve. These parameters were chosen to match the shapes in [12]: $A = 0.0$, $D = 1.0$, $C = 1.0$, $Q = 0.001$, $G = 10.0$. The bulk value, v_{bulk} in (4.10), is calculated as

$$v_{\text{bulk}} = F_{\text{peat}}v_{\text{peat}} + F_{\text{sand}}v_{\text{sand}} + F_{\text{silt}}v_{\text{silt}} + F_{\text{clay}}v_{\text{clay}}, \quad (4.11)$$

where the values of v_i for $i \in \{\text{peat, sand, silt, clay}\}$ are given in Table 1 and are sediment-dependent. The parameter v_{bulk} controls the tail drop-off of the logistic curve (4.10). The freezing/melting temperature, T_f , is a function of pressure and salinity of the pore water. The volume change that occurs during ice-water phase change is ignored. The freezing/melting temperature is calculated according to [38]

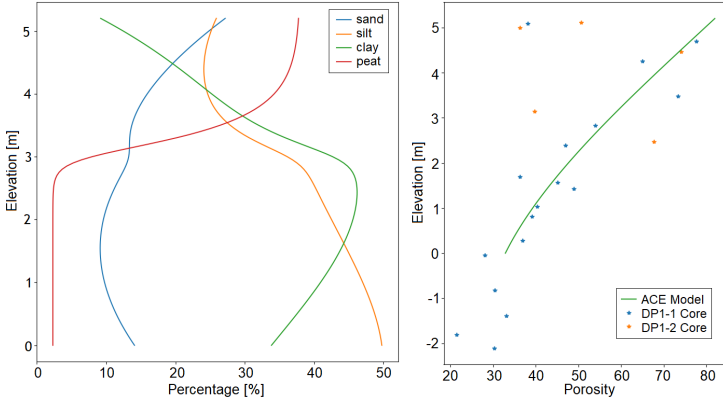


FIGURE 3. Permafrost sediment fractions (left) and effective porosity (right) as a function of depth for an ancient drained lake basin geomorphology. Effective porosity measured core values (stars) are fit with a third order polynomial.

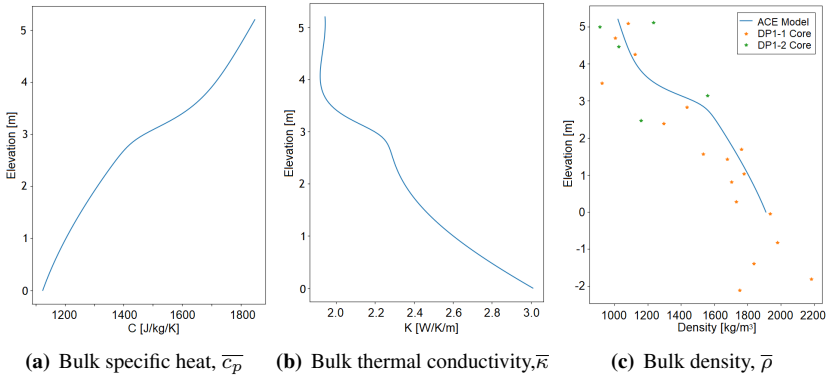


FIGURE 4. Fully frozen (-20°C) permafrost bulk thermal properties as a function of depth for an ancient drained lake basin geomorphology. The bulk density, $\bar{\rho}$, is compared to measured core values in the right-most plot.

using the formula

$$T_f = -5.75 \times 10^{-2}S + 1.70523 \times 10^{-3}S^{1.5} - 2.154996 \times 10^{-4}S^2 - 7.5300 \times 10^{-8}P + 273.15, \quad (4.12)$$

where S is the pore water salinity in parts per thousand (ppt), and P is the local pressure in Pascals (Pa).

As an example, we present the complete thermal material model for an ancient drained lake basin geomorphology typical of the coastal North Slope and studied at Drew Point, Alaska. The field campaign that collected data to support the material model is detailed in [6] and [5]. Figure 3 shows the permafrost sediment fractions (left) and effective porosity (right) as a function of depth. Peat is dominant near the surface, due to the organic layer, but decreases rapidly with depth. The majority

of the permafrost consists of unconsolidated clay and silt. The measured effective porosity generally decreases with depth, and is fit with a third order polynomial (green curve). Furthermore, Figure 4 shows the resulting bulk thermal properties ($\bar{\rho}$ (4.6), \bar{c}_p (4.7), and $\bar{\kappa}$ (4.8)) for fully frozen permafrost as a function of depth. The specific heat capacity generally decreases as a function of depth, mostly due to decreasing contribution of ice or water to the bulk value. On the other hand, thermal conductivity generally increases with depth resulting from increasing contributions of the mineral sediments to the bulk value. The bulk density compares well to measured core values (shown as stars in Figure 4(c)).

5. Erosion by mesh adaptation

A unique feature of the ACE thermo-mechanical terrestrial model described herein is its capability to remove elements within the underlying finite element mesh so as to simulate permafrost erosion. Two ingredients are required for this capability: (1) the definition of appropriate failure criteria to drive the erosion (Section 5.1), and (2) a formal approach for the manipulation of the topology of the underlying finite element meshes as elements are eroded or removed (Section 5.2).

5.1. Failure criteria

The first step in defining an erosion algorithm is establishing the failure criterion (criteria) that leads (lead) to the removal of material from the mesh. Within each time step, the mesh adaptivity infrastructure that we implemented in ALBANY LCM (described in Section 6.2) queries the finite element model to determine if any element satisfies the failure criteria. Currently, there are two failure criteria implemented within ALBANY LCM, the stress criterion and the kinematic criterion, described in more detail in Sections 5.1.1 and 5.1.2, respectively. These criteria define an “erosion variable”, denoted within each element Ω^e as ϕ^e . First, the variables $\phi_{\text{stress}}^{e,\text{qp}}, \phi_{\text{kinematic}}^{e,\text{qp}} \in \{0, 1\}$ are calculated at each integration (quadrature) point (qp) within each finite element Ω^e , according to the formulas (5.2) and (5.7) below. Given this, the erosion variable is obtained for each element Ω^e by summing over all the integration points:

$$\phi^e := \sum_{i=1}^{n_{\text{qp}}} \phi_{\text{stress}}^{e,i} + \sum_{i=1}^{n_{\text{qp}}} \phi_{\text{kinematic}}^{e,i}, \quad (5.1)$$

where n_{qp} denotes the number of quadrature points (we assume this value to be the same across all elements in the mesh). Elements Ω^e in which either of the failure criteria has been met for at least half of the integration points, i.e., $\phi^e \geq \lceil n_{\text{qp}}/2 \rceil$ are marked for removal and subsequently deleted from the finite element mesh topology in the form of the graph representation described in Section 5.2.

5.1.1. Stress failure criterion. The first failure criterion, known as the stress criterion, marks an element for removal when the material within the element reaches a critical value of the stress. This simulates both the development of the niche as well as the initiation and propagation of cracks leading to block failure. In lieu of a loss

of ellipticity analysis at each integration point, which would be computationally prohibitive, we determine a value of the critical stress failure criterion $\phi_{\text{stress}}^{e,i}$ as follows. For each integration point within an element Ω^e ($i = 1, \dots, n^{\text{qp}}$), we set:

$$\phi_{\text{stress}}^{e,i} = \begin{cases} 1, & \text{if } \sigma^{e,i} \geq \sigma_{\text{critical}}; \\ 0, & \text{otherwise.} \end{cases} \quad (5.2)$$

In (5.2), σ_{critical} is a critical value of the stress, in our case $\sigma_{\text{eff}}(T)$ from the material model (4.3), and $\sigma^{e,i}$ is an effective stress, defined as

$$\sigma^{e,i} := \|\mathbf{s}^{e,i}\| \quad (5.3)$$

where

$$\mathbf{s}^{e,i} := \mu \operatorname{dev} \mathbf{b}^{e,i}, \quad \mathbf{b}^{e,i} := (J^{e,i})^{-2/3} \mathbf{F}^{e,i} (\mathbf{C}_{e,i}^{\text{p}})^{-1} (\mathbf{F}^{e,i})^{\text{T}}. \quad (5.4)$$

Here, $\operatorname{dev} \mathbf{A} := \mathbf{A} - \operatorname{vol} \mathbf{A}$, $\operatorname{vol} \mathbf{A} := (\operatorname{tr} \mathbf{A}/3) \mathbf{I}$, and $\mathbf{C}_{e,i}^{\text{p}} := (\mathbf{F}_{e,i}^{\text{p}})^{\text{T}} \mathbf{F}_{e,i}^{\text{p}}$. The variables $\mathbf{F}^{e,i}$ and $\mathbf{F}_{e,i}^{\text{p}}$ denote the deformation gradient and the plastic part of the deformation gradient for element Ω^e and integration point i (see Section 2). Finally, $J^{e,i} := \det(\mathbf{F}^{e,i})$. Note that the value of the critical stress is a function of the ice saturation from (4.4) and (4.5), meaning it varies across elements and integration points.

5.1.2. Kinematic failure criterion. The second failure criterion, the kinematic criterion, removes entire sections of material that has tilted excessively, assuming that the material has fallen as part of block failure. One way to achieve this is to remove elements for which the deformation is large enough that there is a significant rotation of angle of tilt with respect to the reference configuration. Let $\psi^{e,i}$ denote the angle of rotation of an integration point i in element Ω^e . To compute this quantity, we first perform a polar decomposition of the deformation gradient $\mathbf{F}^{e,i}$ corresponding to integration point i in element Ω^e

$$[\mathbf{R}^{e,i}, \mathbf{U}^{e,i}] = \operatorname{polar}(\mathbf{F}^{e,i}), \quad (5.5)$$

where $\mathbf{R}^{e,i}$ and $\mathbf{U}^{e,i}$ are a rotation tensor and a symmetric positive definite tensor, respectively. From this decomposition, the angle of rotation $\psi^{e,i}$ can be extracted from the rotation $\mathbf{R}^{e,i}$ as

$$\psi^{e,i} := \cos^{-1} \left[\frac{1}{2} (\operatorname{tr}(\mathbf{R}^{e,i}) - 1) \right]. \quad (5.6)$$

Given a critical angle ψ_{critical} defining the block erosion, the kinematic failure criterion value corresponding to integration point i in element Ω^e becomes

$$\phi_{\text{kinematic}}^{e,i} = \begin{cases} 1, & \text{if } |\psi|^{e,i} \geq \psi_{\text{critical}}; \\ 0, & \text{otherwise.} \end{cases} \quad (5.7)$$

5.2. Finite element mesh adaptation

In a simulation that requires the removal of material due to physical phenomena such as erosion, the finite element mesh is initially coherent. As the simulation advances, the failure criteria described above are calculated at each integration point each time a specified number of computational steps have been performed. When $\phi^e \geq \lceil n_{qp}/2 \rceil$ for an element Ω^e , the element is removed from the mesh. The continuous evolution of the topology of the mesh is an inherent feature of mesh adaptation element approaches. This evolution involves complex operations on the mesh, with the result that robust three-dimensional implementations that take into account these changes in topology are difficult to develop. A formal approach for the manipulation of the topology of finite element meshes is thus necessary in order to bring the complexities of these operations to a manageable level, and also to avoid the creation of *ad hoc* algorithms that may result in error-prone and inefficient implementations.

In our numerical implementation of element erosion, we employ a so-called complete approach for the topological representation of finite element meshes as graphs. Here, completeness is defined as the ability to generate all topological information from the representation alone, i.e., all adjacency relationships are directly retrievable or derivable from the information contained in the data structure [41, 32, 8, 28]. By recourse to algebraic topology and graph theory, the original n -dimensional cell complex is reduced to a graph, thus greatly decreasing the complexity of the topological manipulations.

6. Thermo-mechanical coupling and implementation

6.1. Sequential thermo-mechanical coupling algorithm

Having described the individual components comprising the ACE thermo-mechanical terrestrial model, we now detail the coupling of these two physics sets. In our formulation, the thermal and mechanical equations are coupled using a sequential iterative approach depicted in Figure 5 and summarized in Algorithm 1. There is no direct

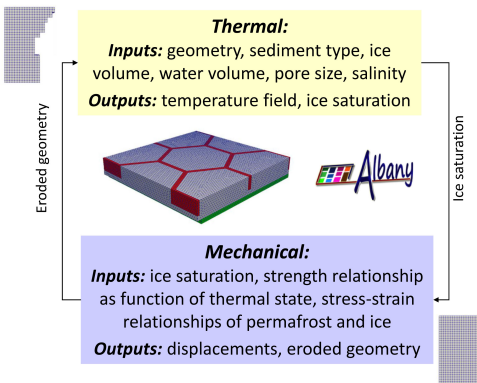


FIGURE 5. Sequential thermo-mechanical coupling

dependence between these equations in the coupling; the dependence is achieved through the material model in the mechanical problem.

We start by defining several parameters, namely the minimum time-step $\Delta t_{min} > 0$, the maximum time-step $\Delta t_{max} > \Delta t_{min}$, the initial time step $\Delta t_{min} \leq \Delta t_0 \leq \Delta t_{max}$, the initial time $t_0 \geq 0$, and the final time $T_{max} > t_0$. We also define two parameters that control the time-step: the “amplification factor” $a_f \geq 1$

and the “reduction factor” $r_f \in [0, 1]$. Lastly, we generate an initial geometry Ω_0 defining the initial region of permafrost.

The coupling algorithm proceeds as follows. We begin by advancing the thermal problem in time by one time-step and extracting from it the ice saturation field $f(T)$. We then proceed to do a mechanical solve corresponding to the same time-step, with the ice saturation field $f(T)$ defining the material model for the mechanics problem ((4.4) or (4.5), depending on the material). The mechanics problem applies the erosion criteria described in Section 5.1 and produces a (possibly new eroded) geometry $\tilde{\Omega}$, provided the time-advancement succeeded. In the case of a successful thermal and mechanical solve, we increment the time-step and repeat the process, this time solving the thermal problem on the new geometry $\tilde{\Omega}$ produced by the mechanical problem. The time-step is incremented based on the previous time-step multiplied by the amplification factor a_f . In the case the time-advancement is not successful, we reduce the time-step by the reduction factor r_f and repeat the process without updating the geometry. Note that our coupling algorithm does not specify which time-integration scheme must be used to advance the thermal and mechanical problems, and the schemes need not be the same, i.e., it is possible to advance one of the problems explicitly and the other implicitly. It turns out that this feature is critical to good computational performance of the coupled model.

Algorithm 1: Sequential thermo-mechanical coupling algorithm.

```

Given:  $\Delta t_0, T_{max}, t_0, \Delta t_{min}, \Delta t_{max}, r_f, a_f, \Omega_0$ ;
Set  $k = 0$ ;
while time  $t_k < T_{max}$  do
    Set  $t_{k+1} = t_k + \Delta t_k$ ;
    Advance thermal problem in  $\Omega_k$  from  $t_k$  to  $t_{k+1}$ , extract ice saturation,  $f_k(T)$ ;
    Advance mechanical problem in  $\Omega_k$  from time  $t_k$  to  $t_{k+1}$  with input ice
      saturation  $f_k(T)$ , which will produce (possibly new eroded) geometry  $\tilde{\Omega}$ ;
    if time advancements are successful then
      | Set  $\Delta t_{k+1} = \min(a_f \Delta t_k, \Delta t_{max})$ ,  $k = k + 1$ ,  $\Omega_k = \tilde{\Omega}$ ;
    else
      | Set  $\Delta t_k = \max(r_f \Delta t_k, \Delta t_{min})$ ;
    end
end

```

We select a sequential coupling algorithm for our thermo-mechanical over a monolithic approach for several reasons. First, due to differences in units, the thermal and mechanical variables have drastically different orders of magnitude. This would make a monolithically coupled thermo-mechanical problem highly ill-conditioned and very difficult/computationally expensive to solve. Additionally, with monolithic coupling, it is not possible to advance the thermal problem forward in time explicitly while time-integrating the mechanical problem implicitly – both problems must be advanced forward in time in the same way: explicitly or implicitly. Both of these approaches have undesirable outcomes. Solving the mechanical problem explicitly is not feasible, as tiny time-steps will be required by the Courant-Friedrichs-Lewy

(CFL) condition; solving the thermal problem implicitly is slow and the physics present challenges for the Newton nonlinear solver. As discussed below in Section 6.2, it is actually straightforward to modify Algorithm 1 such that it emulates monolithic coupling.

6.2. Implementation in Albany LCM code

The terrestrial permafrost model described herein is implemented within a software framework known as ALBANY LCM¹, a fork of ALBANY: an open-source² TRILINOS-based [16] C++ object-oriented, parallel, unstructured-grid, implicit finite element code for solving general partial differential equations, described in more detail in [35].

ALBANY LCM was modified for the targeted application in a number of important ways. The partial differential equations and relevant oceanic and atmospheric boundary conditions defining the thermal problem (Section 3) were added to the code. The mechanical model used in ACE existed already within ALBANY LCM, but had to be modified to work with the appropriate material models for ice and permafrost developed for this application (Section 4.1). It was also necessary to make

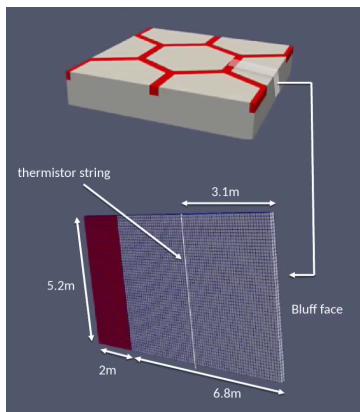


FIGURE 6. Finite element grid of quasi-2D geometry. Red grid cells represent ice; gray cells represent permafrost.

a number of infrastructure changes to the ALBANY LCM code base. Chief among these was the addition of the capability to dynamically erode the underlying mesh geometry (described in Section 5). Another important modification was the introduction of the sequential thermo-mechanical coupling algorithm described in Section 6.1 (Figure 5 and Algorithm 1). Our sequential thermo-mechanical solver was modeled after an existing implementation of the alternating Schwarz method for concurrent multi-scale coupling in solid mechanics [26, 27]. This coupling was achieved through EXODUS output files, which pass relevant information between the thermal and mechanical problems. Specifically, when the thermal problem (line 5 of Algorithm 1) does a time-advancement for time-step $n \in \mathbb{N}$, it writes an EXODUS file with the name `thermal.e-s.n`, which contains the solution for the temperature field as well as the temperature-dependent ice saturation field, $f_k(T)$. Now, when the mechanical problem (lines 6-7 of Algorithm 1) commences its time-integration, it “restarts” from the output file produced by the thermal problem, `thermal.e-s.n`. It is through this EXODUS file that the ice saturation field $f_k(T)$ is passed into the mechanics material model, where it is used to define the mechanics problem. Similarly, once the mechanics problem completes a solve, it writes an exodus file, `mechanics.e-s.n`,

¹ALBANY LCM is available on GitHub: <https://github.com/SNLComputation/LCM>.

²ALBANY is available on GitHub: <https://github.com/SNLComputation/Albany>.

which is used as a “restart” file for the next thermal solve. Since the mechanics problem is the one that performs the mesh erosion, the procedure ensures that the thermal problem always gets the most recent eroded geometry produced by the mechanical solve. For time-integration of the thermal and mechanical problems, we rely on the TEMPUS [29] and PIRO packages from TRILINOS, respectively. In the numerical results presented herein (Section 7), the thermal problem is advanced forward in time using an explicit Forward Euler time-stepper from TEMPUS, and the mechanical problem is advanced forward in time using an implicit trapezoidal rule stepper (i.e., a Newmark scheme with $\gamma = 1/2$ and $\beta = 1/4$) from PIRO. The stable time-step for the coupled algorithm is set by the thermal time-stepper, as it is explicit. Mass lumping is employed in the explicit thermal solve. Note from (3.7) that the mass matrix for the thermal problem changes in time, and therefore needs to be recomputed in each time-step, prior to being lumped.

While the current implementation performs sequential coupling, the framework can achieve a tighter coupling by increasing the number of thermal and mechanical solves within each time-step, following the alternating Schwarz coupling method [26, 27]. Specifically, one can add an additional iteration loop within the `while` loop in Algorithm 1 around the thermal and mechanical advancement steps. Iterating between these problems within a given time-step has the effect of emulating strong (monolithic) coupling, as discussed in [26, 27].

7. Numerical results

In this section, we evaluate the proposed thermo-mechanical terrestrial model for Arctic coastal erosion on a quasi two-dimensional (2D) test case which uses oceanic and atmospheric boundary conditions from Drew Point, Alaska. This evaluation is intended to demonstrate the functionality of the coupled model informed by realistic site-specific data, and is the first step towards a more rigorous quantitative validation, which is reserved for a future publication. Prior to undertaking this evaluation, we verified the numerical methods used in our ACE terrestrial model and their implementation within the ALBANY LCM code base on a simple geometry in which a cuboid comprised of a block of ice material wedged between two blocks of permafrost material is subjected to simultaneous heating and stretching from the top. As shown in [25], all relevant fields (ice saturation, water saturation, temperature and displacement) matched their expected analytical values for this carefully constructed verification test case.

Depicted in Figure 6, the geometry considered here is obtained by taking a cross-section from an archetypal 3D computational domain (representing a typical physical geometry such as the one shown in Figure 1) comprised of hexagonal polygonal permafrost blocks, shown in gray, intersected with a network of ice wedges, shown in red. This quasi-2D domain has dimensions $8.8 \text{ m} \times 5.2 \text{ m}$ in the x - and z -directions. The length of the permafrost polygon is 6.8 m and is adjacent to an ice wedge that is 2 m wide and extends down the entire bluff height. We discretize the computational domain using a uniform linear 8-node hexahedral grid having a resolution of $h = 0.1 \text{ m}$. The domain is two cells thick in the y -direction.

TABLE 2. Physical properties and conditions used for the demonstration simulation.

Property	Value	Unit	Ref./Notes
Mechanical Model Properties			
elastic modulus	0.1×10^9	Pa	[6]
hardening modulus	0	Pa	Elasto-plastic
saturation modulus	0	Pa	Elasto-plastic
saturation exponent	0	—	Elasto-plastic
Poisson ratio	0.2	—	[6]
permafrost bulk density	1700	kg m^{-3}	Fig. 4, median value
ice wedge bulk density	920	kg m^{-3}	
acceleration of gravity	9.806	m s^{-2}	
Critical Failure Criteria			
ice-sediment yield stress	1.5×10^5	Pa	[6]
sediment yield stress	0.705×10^5	Pa	[6]
ice yield stress	3.0×10^6	Pa	[6]
angle of rotation	0.04	radians	[36]
number of failed nodes	5	—	
Thermal Model Properties			
permafrost bulk density	Fig. 4	kg m^{-3}	
ice wedge bulk density	920	kg m^{-3}	
permafrost thermal conductivity	Fig. 4	$\text{W K}^{-1} \text{m}^{-1}$	
ice wedge thermal conductivity	1.6	$\text{W K}^{-1} \text{m}^{-1}$	
permafrost heat capacity	Fig. 4	$\text{J kg}^{-1} \text{K}^{-1}$	
ice wedge heat capacity	2.0×10^3	$\text{J kg}^{-1} \text{K}^{-1}$	
permafrost/ice wedge salinity	0	ppt	
permafrost porosity	Fig. 3	—	
Mechanical Boundary Conditions			
bluff back, bottom	zero displacement	m	
bluff laterals	zero displacement	m	
bluff face, top	zero traction	Pa	
Thermal Boundary Conditions			
bluff back	no heat flux	W m^{-2}	
bluff laterals	no heat flux	W m^{-2}	
bluff bottom	0.08	W m^{-2}	[10]
bluff face, top	time-varying temperature	K	[7],[6]
Thermal Initial Conditions			
bluff temperature	depth-varying	K	[6]

The physical values used in this simulation to specify the ACE terrestrial model properties are given in Table 2. Laboratory experiments performed using permafrost samples from Drew Point, described in detail in [6], informed the numerical values for the mechanical strength parameters. However, the yield stress values used here were lowered relative to the experimental values so as to trigger niche formation earlier in the simulation in this preliminary demonstration. Hence, the values of $\sigma_Y^{\text{ice-sediment}}$ and $\sigma_Y^{\text{sediment}}$ in Table 2 for the stress criterion (5.2) are lower by approximately one order of magnitude from the laboratory experiments. As stated in Section 5 if the critical values are surpassed by at least five nodes in any given element, that element has failed and our dynamic mesh erosion algorithm is applied. A time-step size of 3600 s (1 hour) was chosen based on the CFL condition for the temperature Forward Euler time-stepper (which dictates stability of the coupled problem).

To initialize the ice saturation field within the domain for the material model properties identified in Table 2, a local temperature field beginning on July 25, 2018, 3:07:00 UTC was employed. The initial temperature field, obtained from a vertical string of thermistors placed into the DP1-1 core hole at Drew Point [6], and the freezing curve determined by the material model described in Section 4.2 initialized the ice saturation field which then evolved based upon the atmospheric and oceanographic boundary conditions. At the bottom of the domain, a geothermal heat flux boundary condition of $\sim 0.08 \text{ W/m}^2$ is applied; this was derived from temperature measurements in a deep borehole at Drew Point (DOI/GTN-P Deep Borehole Array project [10]).

The boundary conditions for the mechanical problem are as follows. Symmetry boundary conditions on the face opposite to the bluff (zero displacement in x), on the sides (zero displacement in y), and on the bottom (zero displacement in z). On the top and on the bluff itself, there are zero traction boundary conditions (no loading). The only body force acting on the block is gravity, therefore the acceleration \mathbf{B} in (2.4) is the acceleration of gravity near the surface of the Earth.

To define the time-dependent boundary conditions in our thermal model (3.5)–(3.6), hourly skin temperature (temperature of the ground surface) data are provided by the ERA5 global climate reanalysis product from the European Centre for Medium-Range Weather Forecasts (C3S 2017) [7] at $71^\circ 0' 0'' \text{ N}$, $154^\circ 0' 0'' \text{ W}$. Ocean water level (inclusive of surge, wave height, and run-up), water temperature, and salinity at the permafrost bluff face are output from the oceanographic modeling suite comprised of Wave Watch III, Delft3D-WAVE, and Delft3D-FLOW as described in [6] at $70^\circ 52' 54.66'' \text{ N}$, $153^\circ 53' 55.36'' \text{ W}$. Together, the skin temperature and oceanic boundary conditions are transformed into hourly thermal exposures for each grid elevation as described in [6]. Figure 7 shows a subset of the prescribed temperature values at the bluff face at 0.2, 0.4, and 0.6 m grid elevations. Note that during this time range, at the 0 m elevation, the bluff was exposed to only ocean temperature, while it was exposed to only skin temperature above 0.6 m.

Simulation of the thermo-mechanical terrestrial model given the physical values in Table 2 and subject to the time-dependent boundary conditions shown in Figure

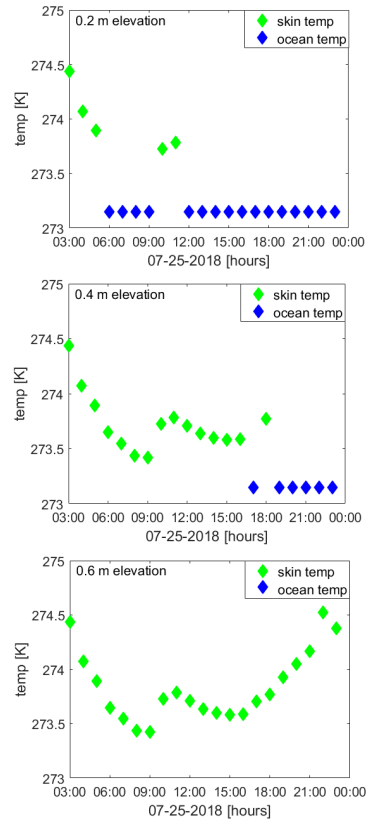


FIGURE 7. Subset of temperature boundary conditions applied to the bluff face at 0.2 m (top), 0.4 m (middle), and 0.6 m (bottom), at 1 hr resolution.

7 progressed for 17 hours until a block collapse event was predicted. A set of time series of model snapshots is shown in Figure 8, with time marching forward from top to bottom. On the left-hand side column of figures, the ice saturation is shown, and on the right-hand side column of figures, we show the grid cell failure state for the same snapshot in time. As the kinematic criterion was not invoked, failure state of the grid cells ranges from 0 to 8, and represents ϕ^e in (5.1).

By inspecting Figure 8, the reader can observe niche progression beginning at the bluff toe, and ultimately progressing inland. A niche that is roughly 3 m deep forms before a block collapse event is predicted, which is similar to the block size observed after a collapse event at Drew Point in late August/early September 2018 [6]. As the niche advances inland, the grid cells experiencing failure are located at the back wall of the niche, driving it to advance deeper. Exposure to the air or the ocean causes the newly exposed permafrost at the boundaries of the niche to thaw.

Once the niche advances ~ 2 m, the tensile stress near the surface of the permafrost block begins to exceed the yield stress of the unfrozen sediment in the thawed surface layer. Two potential regions for tension fracture formation can be seen at the surface: 1) $\sim 2/3$ of the distance inland from the bluff face, and 2) at the ice wedge-permafrost polygon boundary. Block failure at Drew Point has been observed to occur both at ice wedge-polygon boundaries and within the permafrost polygon. These results suggest that both locations may be equally possible given homogeneous mechanical properties. In reality, the location of fracture is probably dependent on which location is weaker. Tension crack development in response to niche formation, as shown in Figure 8, is consistent with the previously published sensitivity study carried out by [36], in which it was shown the regions of maximal tensile stress occur at the surface of the bluff slightly behind the deepest point of the niche. Furthermore, [36] also show regions of maximal compressive state occurring at the top of the back wall of the niche in a 2D cross-section of a permafrost bluff with a prescribed niche geometry, and this can also be seen via visual inspection of the bottom subfigure in Figure 8.

8. Conclusions

In this paper, we introduced the ACE thermo-mechanical terrestrial model for the numerical simulation of Arctic coastal permafrost erosion, and discussed its implementation within the open-source finite element code known as ALBANY LCM. This model is the first numerical modeling framework capable of dynamically modeling all the relevant failure mechanisms of coastal permafrost, including block failure, thermo-abrasion and thermo-denudation. This is accomplished without pre-determined failure planes, critical niche depths or empirical relationships; instead, failure modes develop from constitutive relationships inherent in the underlying finite element model. The ACE thermo-mechanical terrestrial model consists of two components, a solid mechanics component and a thermal component, which are “glued” together via a sequential thermo-mechanical coupling scheme developed in ALBANY LCM for this application. The solid mechanics model calculates 3D stress, strain and displacement fields, which develop in response to a plasticity model of

the underlying permafrost that is controlled by the frozen water content determined by modeling 3D heat conduction and solid-liquid phase change within the thermal model. The coupled thermo-mechanical model has a number of unique characteristics, including: (1) its ability to remove elements from the underlying finite element mesh so as to dynamically simulate permafrost erosion, (2) its unique coupling mechanism, which happens at the level of the underlying constitutive models, and (3) its incorporation of accurate oceanographic and atmospheric boundary conditions at temporal resolutions relevant for the guiding physics to realistically force erosion of a coastal terrestrial permafrost environment. We evaluated the proposed model on a pseudo-realistic problem in which simulated permafrost located at the Drew Point observational site in northern Alaska was exposed to realistic oceanic and atmospheric forcing boundary condition data from July 2018. The model predictions were qualitatively consistent with the observations [6] and predicted a similar region of maximal tensile stress as a previously-published sensitivity study [36] using a mechanics-only terrestrial model.

A quantitative validation study in which the ACE model predictions are compared to available observational data collected during the 2018 and 2019 summer seasons [6] will be the subject of a subsequent publication. Future work will also include the addition of two boundary conditions active at the niche formation: (1) a dynamic ocean water pressure boundary condition expected to alter the state of stress at the bottom of the bluff, and (2) a boundary condition representing salinity-based melting at the portion of the bluff face exposed to the ocean. Further calibration and sensitivity studies will also be carried out using a range of environmental, geomorphological and numerical parameters. Longer term, our objective is to use the ACE model as the microscale component of a multi-scale analysis, in which a statistical meso-scale treatment employs a “catalog” of microscale results to account for the heterogeneity present along Arctic coastlines.

Acknowledgment

This work was funded by the Laboratory Directed Research & Development (LDRD) program at Sandia National Laboratories³. The writing of this manuscript was funded by the third authors’ Presidential Early Career Award for Scientists and Engineers (PECASE). Development of the terrestrial model demonstration was supported by a much larger team from multiple institutions. We would like to acknowledge contributions to the material model by Emily Bristol at University of Texas at Austin, to the mechanical properties by R. Charles Choens at Sandia National Laboratories, of the time-dependent boundary conditions by Christopher Flanary at Integral Consulting, and of the field data by Benjamin Jones at University of Alaska at Fairbanks. We would also like to thank three anonymous reviewers whose insightful comments and suggestions helped us improve this article.

³A multi-mission laboratory managed and operated by National Technology and Engineering Solutions of Sandia, LLC., a wholly owned subsidiary of Honeywell International, Inc., for the U.S. Department of Energy’s National Nuclear Security Administration under contract DE-NA0003525. This paper describes objective technical results and analysis. Any subjective views or opinions that might be expressed in the paper do not necessarily represent the views of the U.S. Department of Energy or the U.S. Government.

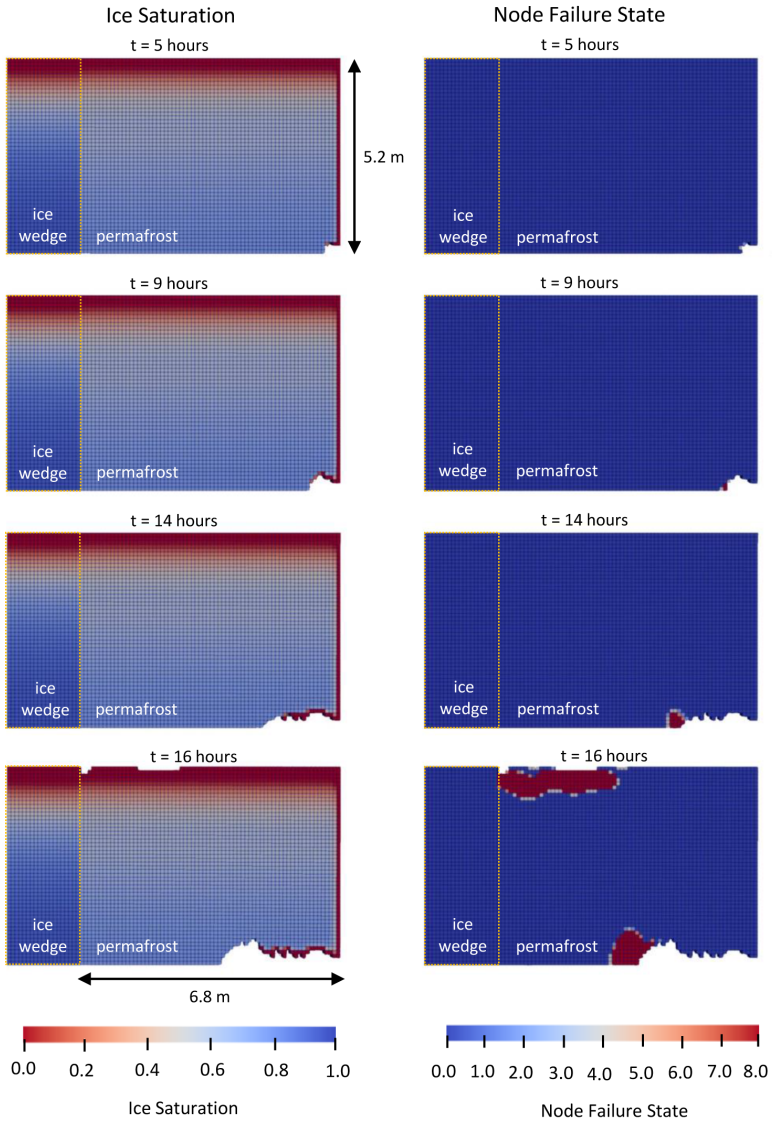


FIGURE 8. Niche formation and node failure state as it progresses on the quasi-2D domain. Niche formation progresses from top to bottom in the columns at 5, 9, 14, and 16 hours of simulation time. Left-hand column shows the ice saturation field (blue represents 100% ice, red represents 0% ice). Right-hand column shows the node failure state of each grid cell (blue, white and red represents 0, 4 and 8 failed integration points, respectively).

References

- [1] M. A. Alzoubi, M. Xu, F. P. Hassani, S. Poncet, and A. P. Sasmito. Artificial ground freezing: A review of thermal and hydraulic aspects. *Tunnelling and Underground Space Technology*, 104:103534, 2020.

- [2] F. Are. Thermal abrasion of sea coasts (Part I). *Polar Geogr & Geol*, 12(1), 1988.
- [3] L. Arenson, S. Springman, and D. Segó. The rheology of frozen soils. *Appl. Rheology*, 17(1):1–14, 2007.
- [4] K. Barnhart et al. Modeling erosion of ice-rich permafrost bluffs along the alaskan beaufort sea coast. *J. Geophys. Res: Earth Surface*, 119(5):1155–1179, 2014.
- [5] E. Bristol, C. Connolly, T. Lorenson, B. Richmond, A. Ilgen, C. Choens, D. Bull, and et al. Geochemistry of coastal permafrost and erosion-driven organic matter fluxes to the Beaufort Sea near Drew Point, Alaska. *Frontiers in Earth Science*, 8, 2011.
- [6] D. Bull et al. Arctic coastal erosion: Modeling and experimentation. Technical report, Sandia National Laboratories, SAND2020-10223, 2020.
- [7] Copernicus Climate Change Service (C3S). ERA5: Fifth generation of ECMWF atmospheric reanalyses of the global climate. Copernicus Climate Change Service Climate Data Store (CDS), <https://cds.climate.copernicus.eu>, 2017.
- [8] W. Celes, G. Paulino, and R. Espinha. A compact adjacency-based topological data structure for finite element mesh representation. *Internat. J. Numer. Meths. Engrg.*, 64(11), 2005. 1529-1556.
- [9] C. Choens. personal communication, April 2019.
- [10] G.D. Clow. Temperature data acquired from the doi/gtn-p deep borehole array on the arctic slope of alaska, 1973–2013. *Earth Syst. Sci. Data*, 6, 2014. 201-218.
- [11] D. Cole. The microstructure of ice and its influence on mechanical properties. *Engineering Fracture Mechanics*, 68(17-18):1797–1822, Dec 2001.
- [12] M. Darrow. Thermal modeling of roadway embankments over permafrost. *Cold Regions Science and Technology*, 65:474–487, 2011.
- [13] M. Darrow, S. Huang, and S. Akagawa. Adsorbed cation effects on the frost susceptibility of natural soils. *Cold Regions Science and Technology*, 55:263–277, 2009.
- [14] T. Gnatowski. Thermal properties of degraded lowland peat-marsh soils, EPSC2016-8105. EGU General Assembly 2016, April 17-22, 2016, Vienna, Austria.
- [15] Günther et al. Short- and long-term thermo-erosion of ice-rich permafrost coasts in the laptev sea region. *Biogeosciences*, 10(6):4297–4318, 2013.
- [16] M. Heroux et al. An overview of trilinos. Technical Report SAND2003-2927, Sandia National Laboratories Report, 8 2003.
- [17] A. Hoque and W. Pollard. Arctic coastal retreat through block failure. *Canadian Geotechnical Journal*, 46(10):1103–1115, 2009.
- [18] A. Hoque and W. Pollard. Stability of permafrost dominated coastal cliffs in the arctic. *Polar Science*, 10(1):79 – 88, 2016.
- [19] T.J.R. Hughes. *The Finite Element Method: Linear Static and Dynamic Finite Element Analysis*. Prentice Hall, 1987.
- [20] N. Kobayashi. Formation of thermoerosional niches into frozen bluffs due to storm surges on the Beaufort sea coast. *J. Geophys. Res-Oceans*, 90(NC6):1983–1988, 1985.
- [21] A. Kruse and M. Darrow. Adsorbed cation effects on unfrozen water in fine-grained frozen soil measured using pulsed nuclear magnetic resonance. *Cold Regions Science and Technology*, 142:42–54, 2017.
- [22] H. Lantuit et al. The Arctic coastal dynamics database: A new classification scheme and statistics on arctic permafrost coastlines. *Estuaries and Coasts*, 35(2):383–400, 3 2012.
- [23] E. Lee. Elastic-plastic deformation at finite strains. *J. Appl. Mech.*, 36(1):1–6, 1969.

- [24] J. Marsden and T. Ratiu. *Introduction to Mechanics and Symmetry: A Basic Exposition of Classical Mechanical Systems*. Springer-Verlag, New York, 1999.
- [25] A. Mota, J. Frederick, C. Choens, D. Bull, and I. Tezaur. Development of a strongly-coupled thermo-mechanical model of permafrost for the simulation of arctic coastal erosion. European Seminar on COmputing (ESCO) 2020, June 8-12, 2020.
- [26] A. Mota, I. Tezaur, and C. Alleman. The Schwarz alternating method. *Comput. Meth. Appl. Mech. Engng.*, 319:19–51, 2017.
- [27] A. Mota, I. Tezaur, and G. Philipot. The Schwarz alternating method for transient solid dynamics. *Comput. Meth. Appl. Mech. Engng. (under review)*, 2020.
- [28] Alejandro Mota, Jaroslaw Knap, and Michael Ortiz. Fracture and fragmentation of simplicial finite element meshes using graphs. *INTERNATIONAL JOURNAL FOR NUMERICAL METHODS IN ENGINEERING*, 73(11):1547–1570, MAR 12 2008.
- [29] C. Ober, S. Conde, and R. Pawlowski. Tempus: Time integration package. trilinos.github.io/tempus.html, February 2018.
- [30] M.T. O’Conner, M.B. Cardenas, S.B. Ferencz, Y. Wu, B.T. Neilson, J. Chen, and G.W. Kling. Empirical models for predicting water and heat flow properties of permafrost soils. *Geophysical Research Letters*, 47(11), 2020.
- [31] T. Ravens et al. Process-based coastal erosion modeling for Drew Point, North Slope, Alaska. *J. Waterway Port Coastal Ocean Eng.*, pages 122–130, 2012.
- [32] J.F. Remacle and M.S. Shephard. An algorithm oriented mesh database. *Internat. J. Numer. Meths. Engng.*, 58(2):349–374, 2003.
- [33] E. C. Robertson. Thermal properties of rocks. U.S. Geological Survey Open-File Report 88-441, 1988.
- [34] D. Russell-Head. The melting of free-drifting icebergs. *Ann. Glaciol.*, 1:119–122, 1980.
- [35] A. Salinger et al. Albany: Using agile components to develop a flexible, generic multi-physics analysis code. *Int. J. Multiscale Comput. Engng.*, (4):415–438, 2016.
- [36] M. Thomas et al. Geometric and material variability influences stress states relevant to coastal permafrost bluff failure. *Frontiers in Earth Science*, 8:143, 2020.
- [37] P. Tryde. Physics and Mechanics of Ice. *Naturwissenschaften*, 67(11):556–559, 1980.
- [38] UNESCO. Algorithms for the computation of fundamental properties of seawater. *UNESCO Technical Papers in Marine Science*, 44:1–55, 1983.
- [39] H. Walker. Permafrost and coastal processes. In Proceedings of the Fifth International Conference on Permafrost (Vol. 3, pp. 35–42), 11 1988.
- [40] X. Wan and Z. Yang. Pore water freezing characteristic in saline soils based on pore size distribution. *Cold Regions Science and Technology*, 173, 2020.
- [41] K. Weiler. *The Radial Edge Structure: A Topological Representation for Non-Manifold Geometric Boundary Modeling*, pages 3–36. North-Holland, 1988.
- [42] F. White et al. Theoretical estimates of various mechanism involved in iceberg deterioration in the open ocean environment. U.S. Coast Guard Technical Service Information Service Publication CG-D-62-8081-20571, 126, 1980.
- [43] C. Wobus et al. Thermal erosion of a permafrost coastline: improving process-based models using time-lapse photography. *Arctic Antarctic Alpine Res.*, 43:474–484, 2011.